# Fuel Optimal Propulsive Maneuver of an Experimental Structure Exhibiting Spacelike Dynamics

J. L. Meyer* and L. Silverberg†

North Carolina State University, Raleigh, North Carolina 27695-7921

The implementation of four fuel-optimal methods for propulsive maneuver of space structures is described. Toward this end, an experimental structure that possessed spacelike dynamics was fabricated and used to test the previously mentioned fuel optimal methods. The results given highlight the differences among fuel optimal methods for propulsive maneuver of space structures, their relative strengths and weaknesses, and the sources of errors.

## I. Introduction

SEVERAL laboratories have developed experimental facilities[1-4] to study vibration suppression[5-14] and maneuver[15-21] of large space structures. The experimental structures were designed to exhibit spacelike dynamics and to possess adequate control authority. Unfortunately, the gravity environment induces unwanted elastic deformations unless the elastic deformations are confined to the plane perpendicular to gravity. Furthermore, when fuel supplies, sensor electronics, and actuator electronics are placed onboard the experimental structure, the control authority can decrease to prohibitively low levels. This paper describes an experimental structure that undergoes spacelike rigid-body motions (five out of the six degrees of freedom) and in-plane elastic motions and that possesses control authority large enough to overcome out-of-plane gravity induced disturbances. This paper also describes four fuel optimal methods for rest-to-rest maneuvers and highlights the relative sources of errors.

The experimental structure consisted of four spring steel beams assembled into an X shape (Fig. 1a). This configuration was studied previously[17-20] but was restricted to in-plane (perpendicular to gravity) motions. The experimental structure described here underwent three rigid-body rotational motions (one in-plane and two out-of-plane) and two rigid-body transitional motions (in-plane). The out-of-plane rigid-body translational motion was omitted. The experimental structure also underwent elastic deformations in the plane of the X. The control authority was maximized by placing the actuators in clusters at the tips of the beams and by minimizing component weights.

The experimental structure was designed for the development and verification of advanced fuel and time optimal strategies for the maneuver of large space structures. Furthermore, it is the third in a series of structures fabricated by the authors for the same purpose. The first structure underwent in-plane elastic motions[14] (no rigid-body motions) and the second structure underwent one in-plane rigid-body rotational motion (slewing) and one significant in-plane elastic motion.[21] Related developments in fuel and time optimal control are found in Refs. 22–25. This paper focuses on the design of the experimental structure and on the development and verification of several new strategies for near fuel optimal control.

Section II gives a detailed description of the experimental setup and Sec. III presents the system dynamics. The formulation of four fuel optimal control strategies is given in Sec. IV. These are an open-loop control for out-of-plane maneuver, a hybrid control for

in-plane maneuver and vibration suppression, an open-loop control for in-plane rest-to-rest maneuver, and an augmented open-loop control for in-plane rest-to-rest maneuver. Section V describes the air thrust actuation and Sec. VI describes the rigid-body sensing and the elastic-body sensing. Finally, Sec. VII presents and discusses the experimental results.

## II. Experimental Setup

The experimental setup consisted of four spring steel beams connected together at a central hub at right angles to each other to form an X (Fig. 1a). The central hub enabled free rotations about three body-fixed axes. A cluster of four air thrust actuators were located at the tip of each beam (Fig. 1b). Strain gauges measured root curvature at the point where each beam meets the hub. A 3-axis rate sensor mounted to the hub measured angular rates of the 3 body-fixed axes (Fig. 1c). The system was suspended from above by a hollow aluminum rod connected to a gimbaled joint. A joystick, connected to the rod near the suspension point, measured rigid-body displacements (Fig. 1d). The system parameters are given in Table 1.

Table 1  System parameters

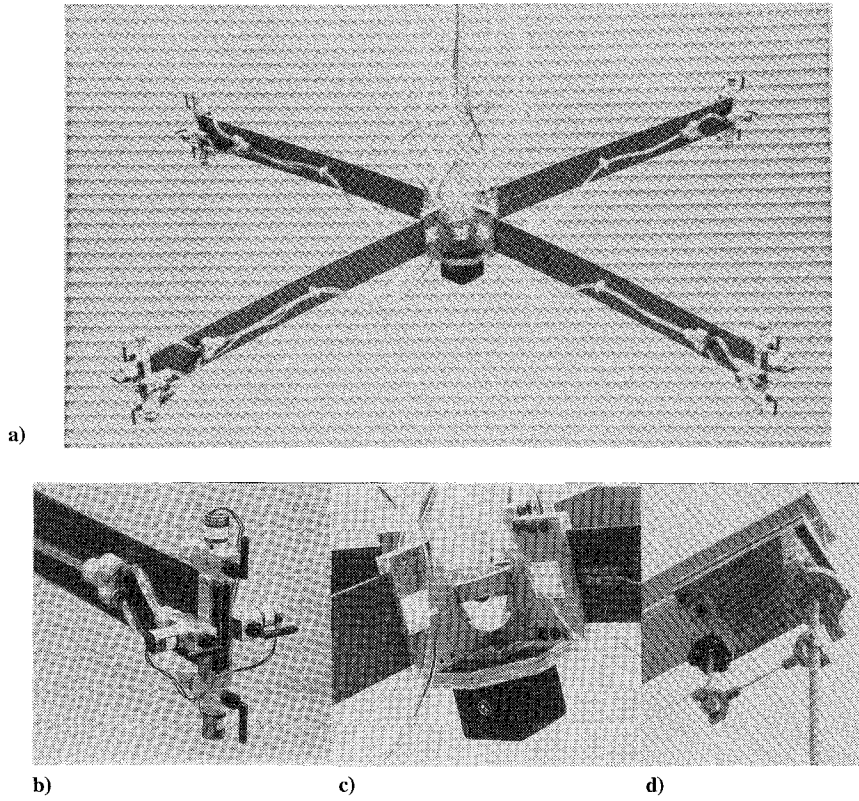| Component | Parameter | Symbol | Value | Units |
|---|---|---|---|---|
| Beam element | Length | $L$ | 28.125 | in. |
| | Width | | 3.0 | in. |
| | Thickness | $T$ | 0.0624 | in. |
| | Elastic modulus | $E$ | $24.25 \times 10^6$ | psi |
| | Area moment of inertia | $I$ | $6.55 \times 10^{-5}$ | in.$^4$ |
| | Mass per unit length | $\rho$ | 0.020 | slug/ft |
| Hub | Diameter | | 8.0 | in. |
| | Height | | 4.0 | in. |
| | Mass | | 0.088 | slug |
| Air thrust actuators | Location | $x_\ell$ | 31.875 | in. |
| | Mass | | 0.019 | slug |
| Angular rate transducer | Location | $x$ | 0.0 | in. |
| | | $y$ | 0.0 | in. |
| | | $z$ | −3.8125 | in. |
| | Mass | | ˙0.026 | slug |
| Strain gauge | Location | | 4.0 | in. |
| | Mass | | 0.000 | slug |
| C.G. adjustment plates | Location | $x$ | 0.0 | in. |
| | | $y$ | 0.0 | in. |
| | | $z$ | −2.5 | in. |
| Full system | Structural damping | $\zeta$ | 0.00374 | |
| | In-plane mass moment of inertia | $I_\psi$ | 1.146 | slug·ft$^2$ |
| | In-plane hinge friction coefficient | $C_\psi$ | 0.08 | lbf·ft·s |
| | Out-of-plane mass moment of inertia | $I_\phi, I_\theta$ | 0.604 | slug·ft$^2$ |
| | Out-of-plane hinge friction coefficient | $C_\phi, C_\theta$ | 0.27 | lbf·ft·s |

Fig. 1  Experimental setup: a) X-shaped beam assembly, b) actuator cluster, c) hub mount with rate sensor, and d) upper mount with joystick.

The use of low cross section spring steel beams produced high in-plane flexibility with minimum mass. The central hub was fabricated from aluminum, and the rotation joint design was based on a concentric rotating rings concept similar to gimbaled gyros. A precision bearing at the center of the inner ring allowed the system to rotate about the axis perpendicular to the plane defined by the X. The overall hub mass was minimized along with the surface contact area at each of the hinge points. The design of the joint at the upper suspension point was similar to the design of the joint at the hub with the exception that no axial rotations of the aluminum rod were permitted. A two-axis joystick sensor was positioned near the top connection point. The joystick sensor was designed to shadow the motion of the aluminum rod via a follower connection to the rod. The joystick outputted displacement measurements of the central hub. Each actuator cluster was composed of four air fed solenoid valves fitted with directional nozzles. The valves were constructed of aluminum and the supply line connections and nozzles were high-strength plastic capable of handling pressures up to 100 psi. The angular rate sensor was compact and mounted on the central hub near the center of the axis of rotation to minimize the system inertia and the cross-axis coupling. The strain gauges mounted on each beam element measured curvature at the root from which elastic deflections relative to a line tangent to the beam at the root were computed. The angular rate sensor, the joystick sensor, and the four strain gauges provided complete system observability. The required electronics and the air supply were tethered to the system to reduce the system mass that, in turn, preserved the high-control authority of the system. Two steel adjustment plates were mounted on the hub for center of gravity adjustments. The significant elastic frequencies of the overall structure were appreciably lower than the maximum data acquisition sampling rates and far removed from the actuator dynamics.

## III.  System Dynamics

The experimental structure was modeled as four interconnected free-free Bernoulli–Euler beams with tip masses representing actuator clusters and with a mass at the root representing the hinge mount and the angular rate sensor. The geometric boundary conditions
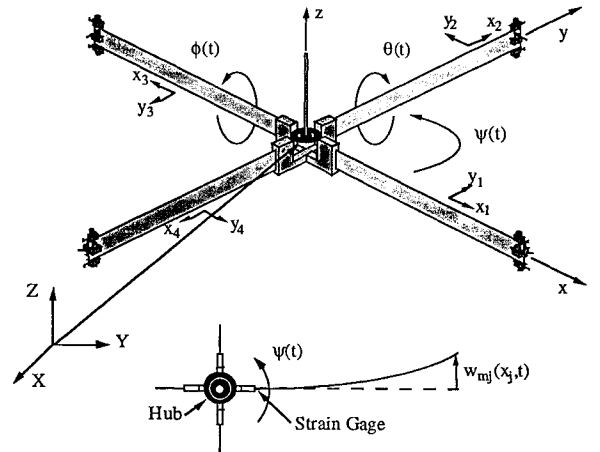


Fig. 2  Coordinate system.

consisted of 90-deg connections between adjacent beams at their roots to form an X.

The in-plane dynamics of the $j$th free-free beam are represented by the differential equations of motion

$$I_{\psi j}\ddot{\psi}_j(t) = \tau_{\psi j}(t) = u_j(t) \cdot x_\ell \tag{1}$$

$$\rho(x_j)\frac{\partial^2 w_j(x_j, t)}{\partial t^2} + C\frac{\partial w_j(x_j, t)}{\partial t}$$

$$+ \frac{\partial^2}{\partial x_j^2}\left(EI(x_j)\frac{\partial^2 w_j(x_j, t)}{\partial x_j^2}\right) = u_j(t)\delta(x_j - x_\ell) \tag{2}$$

where $w_j(x_j, t)$ denotes the elastic displacement of the $j$th member at point $x_j$ and time $t$. As shown in Fig. 2, the elastic displacement is measured relative to a beam-fixed coordinate system in which the $x_j$ axis is tangent to the slope at the hub connection point. The hub rotation angle is denoted by $\psi_j(t)$ and the applied torque about the center of the hub is denoted by $\tau_{\psi j}(t)$. The actuator moment
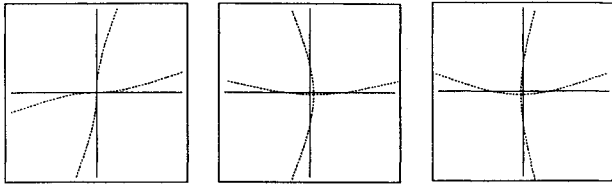
Fig. 3  Lowest three elastic modes.

arm is $x_\ell$ and the beam length is $L$. The in-plane mass moment of inertia of the $j$th beam about the center of the hub is denoted by $I_{\psi j}$, the mass per unit length by $\rho(x_j)$, the stiffness by $EI(x_j)$, and the structural damping operator by $C$. The damping operator, which includes both structural damping and air damping, is of the proportional type thereby preserving the normal mode characteristics of the vibration. This assumption is quite reasonable in the case of light damping. The rates of rotation are assumed to be small, which in turn leads us to neglecting the kinematic coupling between the rigid- and flexible-body equations of motion. The beam length, actuator moment arm, mass moment of inertia, mass per unit length, stiffness, and structural damping of each member are equal so that the beam identifying subscript may be neglected. The air thrust actuator applies the point force $u_j(t)$ and the corresponding spatial impulse function is $\delta(x_j - x_\ell)$.

The normal modes and frequencies of the system are computed by solving the associated eigenvalue problem

$$\omega_i^2 \rho(x_j)\phi_{ij}(x_j) = \frac{\mathrm{d}^2}{\mathrm{d}x^2}\left(EI\frac{\mathrm{d}^2\phi_{ij}(x_j)}{\mathrm{d}x^2}\right)$$

$$(j = 1, 2, 3, 4; \quad i = 0, 1, 2, \ldots)$$

subject to the geometric boundary conditions at the hub. Arranging the modes $\phi_{ij}(x_j)$ ($i = 0, 1, 2, \ldots$) and the corresponding frequencies $\omega_i$ ($i = 0, 1, 2, \ldots$) in ascending order, the lowest three modes become the two rigid-body translational modes and the rigid-body slewing mode with associated frequencies of zero ($\omega_0 = 0$). No translational control will be performed in this paper so that the slewing mode, denoted by $\phi_0(x)$, will be the only rigid-body mode controlled. The first three elastic modes, denoted by $\phi_1(x)$, $\phi_2(x)$, and $\phi_3(x)$, and the associated frequencies $\omega_1$, $\omega_2$, and $\omega_3$ will also be controlled. The solution of the eigenvalue problem is obtained by the Rayleigh–Ritz method. The admissible functions for each beam are $\varphi_r(y) = (y/L)^{r-1}$, ($r = 1, 2, \ldots, 10$) for translations, rotations, and bending displacements in the $y$ direction, and $\varphi_s(x) = (x/L)^{s-1}$, ($s = 1$) for axial displacements in the $x$ direction. The associated mass and stiffness matrices for each element are[26]

$$m_{rs} = \int_0^L \rho(x)\varphi_s(x)\varphi_r(x)\,\mathrm{d}x$$

$$k_{rs} = \int_0^L EI(x)\varphi_s''(x)\varphi_r''(x)\,\mathrm{d}x$$

The beam's mass and stiffness matrices are then assembled to form the system mass and stiffness matrices. The lowest three elastic modes are shown in Fig. 3.

Neglecting the influence of the fourth and higher elastic modes, the $j$th beam's elastic displacement is

$$w_j(x_j, t) = \sum_{i=1}^{3} \phi_{ij}(x_j)q_i(t), \qquad (j = 1, 2, 3, 4) \quad (3)$$

where $q_i(t)$ is the modal displacement of the $i$th mode and $\phi_{ij}(x_j)$ is the $i$th mode shape for the $j$th member at $x_j$. Substituting Eq. (3) into Eq. (2), premultiplying by $\phi_{ij}(x_j)$ and integrating over the domain, we obtain the modal equations of motion[26]

$$\ddot{q}_i(t) = -2\alpha_i\dot{q}_i(t) - (\omega_i^2 + \alpha_i^2)q_i(t) + \sum_{j=1}^{4}\phi_{ij}(x_j)u_j(t) \quad (4)$$

where $\alpha_i$ is a damping rate that has been introduced. Equations (1) and (4) are recast in the form of the linear state equations

$$\dot{x}(t) = Ax(t) + Bu(t) \quad (5)$$

where

$$x(t) = [\psi(t) \quad \dot{\psi}(t) \quad q_1(t) \quad \dot{q}_1(t) \quad q_2(t) \quad \dot{q}_2(t) \quad q_3(t) \quad \dot{q}_3(t)]^T$$

$$u(t) = [u_1(t) \quad u_2(t) \quad u_3(t) \quad u_4(t)]^T$$

$$A = \begin{bmatrix} a_0 & 0 & 0 & 0 \\ 0 & a_1 & 0 & 0 \\ 0 & 0 & a_2 & 0 \\ 0 & 0 & 0 & a_3 \end{bmatrix}, \qquad B = [b_0 \quad b_1 \quad b_2 \quad b_3] \quad (6)$$

$$a_0 = \begin{bmatrix} 0 & 1 \\ 0 & 0 \end{bmatrix}, \qquad a_i = \begin{bmatrix} 0 & 1 \\ -(\omega_i^2 + \alpha_i^2) & -2\alpha_i \end{bmatrix}$$

$$\text{for} \quad i = 1, 2, 3$$

and

$$b_j = [0 \quad x_\ell/I_\beta \quad 0 \quad \phi_{1j}(x_\ell) \quad 0 \quad \phi_{2j}(x_\ell) \quad 0 \quad \phi_{3j}(x_\ell)]^T$$

The out-of-plane pitch dynamics are represented by the differential equations of motion

$$I_\theta\dot{\Omega}_\theta(t) = -C_\theta\Omega_\theta(t) + \tau_\theta(t) \quad (7)$$

which can be rewritten in the state form given in Eq. (5) in which

$$A = \begin{bmatrix} 0 & 1 \\ 0 & -C_\theta/I_\theta \end{bmatrix}, \qquad B = \begin{bmatrix} 0 \\ 1/I_\theta \end{bmatrix} \quad (8)$$

where $x(t) = [\theta(t) \quad \Omega_\theta(t)]^T$, $u(t) = \tau_\theta(t)$, $\theta(t)$ is the pitch angle, $C_\theta$ is the damping factor for hinge friction, $I_\theta$ is the mass moment of inertia about the hub, and $\tau_\theta(t)$ is the applied torque about the hub. This completes the formulation of the in-plane dynamics [Eqs. (5) and (6)] and the out-of-plane dynamics [Eqs. (5) and (8)] of the experimental structure.

## IV. Fuel Optimal Control

We now develop four methods for the fuel-optimal maneuver of the experimental structure.

### Open-Loop Out-of-Plane Maneuver

Fuel optimal propulsive actuation is ideally impulsive.[22] The fuel function is

$$Fu = \int_{t_0}^{t_f} |u(t)|\,\mathrm{d}t \quad (9)$$

Associated with minimizing Eq. (9), we define the control determining function $g(\eta, t) = \eta^T e^{-At}B$ where $\eta$ is a $2 \times 1$ vector contained in the hyperplane $H = (\eta: \eta^T y = 1)$ and where $y = e^{-At_f}x_f - x_0$ is the reachable state in which $x_0 = x(t_0)$ and $x_f = x(t_f)$ denote the initial and final states, respectively. The state transition matrix for the out-of-plane dynamics of the experimental structure is given by

$$e^{-At} = \begin{bmatrix} 1 & (I_\theta/C_\theta)(1 - e^{C_\theta t/I_\theta}) \\ 0 & e^{C_\theta t/I_\theta} \end{bmatrix} \quad (10)$$

The solution to the fuel optimal control problem is determined by selecting $\eta$ such that

$$\alpha^* = \min_{\eta \in H} \sup_{t_0 \le t \le t_f} |g(\eta, t)| \quad (11)$$

where $\alpha^*$ is defined as the fuel coefficient. The minimum amount of fuel is $Fu^* = 1/\alpha^*$. The solution to Eq. (11) yields the optimal normal vector $\eta^*$ resulting in a control of the form

$$u^*(t) = \Delta^T c/\alpha^* \quad (12)$$

where $\Delta$ is an $N \times 1$ vector of impulses and $c$ is an $N \times 1$ vector of impulse coefficients given by

$$\Delta = \left\{ \mathrm{sgn}\left[g\left(\eta^*, \tau_1\right)\right]\delta(t - \tau_1) \cdots \mathrm{sgn}\left[g\left(\eta^*, \tau_N\right)\right]\delta(t - \tau_N)\right\}^T$$

$$c = [c_1 \quad c_2 \quad \cdots \quad c_N]^T \tag{13}$$

where $\delta(t - \tau_i)$ is a unit impulse at time $\tau_i$. The impulse coefficients are nonnegative constants that satisfy $1 = \sum_{i=1}^{N} c_i$. The control determining function for out-of-plane rest-to-rest maneuver is

$$g(\eta, t) = (1/C_\theta)(1 - e^{C_\theta t/I_\theta})\eta_1 + (1/I_\theta)e^{C_\theta t/I_\theta}\eta_2 \tag{14}$$

The open-loop maneuver is defined by $x_0 = [\theta_f - \theta_0 \ 0]^T$ and $x_f = 0$ that, after imposing the hyperplane constraint yields $\eta_1 = -(\theta_f - \theta_0)^{-1}$. By inspection of Eqs. (11) and (14), we obtain

$$\eta^* = \left[ -(\theta_f - \theta_0)^{-1}\frac{I_\theta}{C_\theta(\theta_f - \theta_0)} \cdot \frac{(e^{C_\theta t_f/I_\theta} - 1)}{(e^{C_\theta t_f/I_\theta} + 1)} \right]^T$$

$$\alpha^* = \left| \frac{1}{C_\theta(\theta_f - \theta_0)} \cdot \frac{(e^{C_\theta t_f/I_\theta} - 1)}{(e^{C_\theta t_f/I_\theta} + 1)} \right| \tag{15}$$

The solution to the fuel optimal rest-to-rest control problem yields $N = 2$ in which $\tau_1 = t_0$ and $\tau_2 = t_f$. The impulse coefficients $c_1$ and $c_2$ are determined next. The solution to Eq. (5) is

$$x(t) = e^{At}\left[ x(t_0) + \int_{t_0}^{t} e^{-As}Bu(s)\,\mathrm{d}s \right] \tag{16}$$

Substituting Eq. (12) into Eq. (16) and evaluating the result at time $t_f$ yields a set of simultaneous linear algebraic equations

$$Pc = Q$$

$$Q = \begin{bmatrix} y \\ 1 \end{bmatrix}, \qquad P = \begin{bmatrix} \dfrac{1}{\alpha^*}\displaystyle\int_{t_0}^{t_f} e^{-At}Bg^T\,\mathrm{d}t \\ 1 \end{bmatrix}, \qquad c = \begin{bmatrix} c_1 \\ c_2 \end{bmatrix} \tag{17}$$

where the $1$ in the $P$ matrix is a $2 \times 1$ vector of ones. In the case of fuel optimal open-loop rest-to-rest maneuver, the solution to Eq. (17) results in $c_1 = [1 + \exp(-C_\theta t_f/I_\theta)]^{-1}$ and $c_2 = [1 + \exp(C_\theta t_f/I_\theta)]^{-1}$. Note that if no frictional damping had been included in the system model, the coefficients would be equal to $\frac{1}{2}$, however, the fuels required to complete the maneuvers would still be identical.

## Hybrid In-Plane Maneuver

The numerical difficulties encountered in computing the fuel optimal solution of higher-order systems are associated with solving Eq. (11). The nonlinearities and discontinuities prevent Eq. (11) from being solved easily by rudimentary numerical techniques. Instead, one must resort to numerical schemes that can require a computation time that quickly becomes prohibitive as the order of the system increases.[23]

With low-order systems these problems are readily overcome. Therefore, an approach to rendering a near fuel optimal solution for higher-order systems proceeds by extending the properties determined for fuel optimal control of these low-order systems to similar higher-order systems.[14,24,25]

It has been shown for a simple harmonic oscillator that the fuel required for vibration suppression is minimized when a single control force is applied in a direction that opposes the velocity with a magnitude equal to the system's momentum and at a time defined by the intersection of two events. The first event occurs when the oscillator experiences a peak velocity and the second occurs when the oscillator experiences a minimum displacement. For the harmonic oscillator, these two events occur simultaneously, in which case it is sufficient to consider only one of these events. For higher-order systems these events do not necessarily coincide, in which case both events must be considered in order to determine the times at which they intersect. The first event is approximated by a region of peak velocity,

and the second event is approximated by a region of minimum displacement. Furthermore, it has been shown that the single impulse can be replaced by a series of constant level finite duration pulses applied at the intersection of the two events. These properties are slight approximations that increase the fuel consumed only marginally. This method is known as impulse damping control (IDC).[25]

In view of the preceding discussion, a hybrid control is developed that uses the exact solution for the fuel optimal rigid-body maneuver and IDC for fuel optimal vibration suppression. Thus, at the completion of the rigid-body maneuver, IDC is implemented to quench the residual vibration. The occurrences of peak local velocities and minimum local displacements are approximated by comparing the structure's elastic displacement and velocity with its respective running-in-time standard deviations. When the elastic velocity is greater than its scaled standard deviation, it is considered in a region of peak velocity. Also, when the elastic displacement is below its scaled standard deviation, it is considered in a region of minimum displacement. The standard deviations are computed over a running-in-time finite duration rectangular window. The indicated two events for each actuator location are

$$E_{1j}(x_\ell): |w_j(x_\ell, t)| \leq \mu_{w_j}\sigma_{w_j}(x_\ell, t)$$

$$E_{2j}(x_\ell): |\dot{w}_j(x_\ell, t)| \geq \mu_{\dot{w}_j}\sigma_{\dot{w}_j}(x_\ell, t) \tag{18}$$

where $w_j(x_\ell, t)$ and $\dot{w}_j(x_\ell, t)$ are the elastic displacement and velocity at the $j$th actuator location, $\sigma_{w_j}(x_\ell, t)$ and $\sigma_{\dot{w}_j}(x_\ell, t)$ are the associated running-in-time standard deviations, and $\mu_{w_j}$ and $\mu_{\dot{w}_j}$ are the respective scale factors for the standard deviations.

This leads to a control law of the form

$$u_j(t) = \begin{cases} -U_j\mathrm{sgn}[\dot{w}(x_\ell, t)] & E_{1j}(x_\ell) \cap E_{2j}(x_\ell) \\ 0 & \text{otherwise} \end{cases} \tag{19}$$

## Open-Loop In-Plane Maneuver

The third approach is developed in the modal space wherein impulsive modal forces are transformed to yield quantized control forces.[27] An initial and final modal pulse controls each mode in which the first modal pulse for each mode occurs at $t_0 = 0$. A single actuator will initiate the maneuver and all four actuators will be used throughout the remaining time of the maneuver. At appropriate times during the maneuver, each mode is removed from the response such that at the final maneuver time $t_f$ the structure will have achieved its target angle and will be at rest.

The maneuver is initiated by an impulse at $t_0 = 0$ of the form $u(0) = \hat{U}(0)\delta(t)$ in which $\hat{U}^T(0) = [u_0 \ 0 \ 0 \ 0]$. The control force is separated into its modal components by

$$\hat{U}_j(t) = \sum_{i=0}^{3} \phi_{ij}(x_\ell)\hat{Q}_i(t) \qquad (j = 1, 2, 3, 4) \tag{20}$$

where $\hat{U}(t) = [\hat{U}_1(t) \ \hat{U}_2(t) \ \hat{U}_3(t) \ \hat{U}_4(t)]^T$ and $\hat{Q}_i(t)$ is the $i$th modal impulse.

The predicted values of the mode shapes at $x_\ell$ are

$$\phi_0 = \begin{bmatrix} 2.69629 \\ 2.69629 \\ 2.69629 \\ 2.69629 \end{bmatrix}, \qquad \phi_1 = \begin{bmatrix} 0.28093 \\ -0.28093 \\ 0.28093 \\ -0.28093 \end{bmatrix}$$

$$\phi_2 = \begin{bmatrix} 0.15863 \\ 0.24582 \\ -0.15863 \\ -0.24582 \end{bmatrix}, \qquad \phi_3 = \begin{bmatrix} 0.24582 \\ 0.15863 \\ -0.24582 \\ -0.15863 \end{bmatrix} \tag{21}$$

in which $\phi_i = [\phi_{i1}(x_\ell) \ \phi_{i2}(x_\ell) \ \phi_{i3}(x_\ell) \ \phi_{i4}(x_\ell)]^T$ $(i = 0, 1, 2, 3)$. In Eq. (21) we observe that the mode shapes at $x_\ell$ are orthogonal,

that is, $\phi_r^T \phi_s = 0$ for $r \neq s$. Invoking the orthogonality conditions, we obtain from Eq. (20) the modal forces at $t = 0$

$$\hat{Q}_i(0) = \frac{\phi_i^T \hat{U}(0)}{\phi_i^T \phi_i} \tag{22}$$

Now consider the rigid body mode whose equation of motion is

$$\ddot{\psi}(t) = \tau_\psi(t)/I_\psi$$

where $\tau_\psi(t) = x_\ell \hat{U}^T(t)\Delta_0$ is the control torque and $\Delta_0 = [\delta(t - t_0) \; \delta(t - t_{0f})]^T$ is the $2 \times 1$ vector of unit impulses associated with rigid-body control where $t_0$ is the initial time and $t_{0f}$ is the time at which the rigid-body pulse is applied to remove the rigid-body component of the response. The solution to the rigid-body equation of motion is of the form

$$\psi(t) = c_{01} + c_{02}t \tag{23}$$

where $c_{01}$ and $c_{02}$ are coefficients to be determined. The initial and final conditions are $\psi(t_0) = \psi_m, \dot{\psi}(t_0) = 0$, and $\psi(t_{0f}) = \dot{\psi}(t_{0f}) = 0$. From Eq. (23)

$$\hat{U}(t_0) + \hat{U}(t_{0f}) = Q_0(t_0) + Q_0(t_{0f}) = 0$$
$$\psi_m(I_\psi/x_\ell) = \hat{U}(t_0) \cdot (t_{0f} - t_0) \tag{24}$$

The magnitude of the initial impulse is now determined from Eqs. (22–24):

$$u_0 = \frac{\psi_m I_\psi}{(t_0 - t_{0f})x_\ell} \tag{25}$$

Now consider the modal equation of motion of the $i$th elastic mode

$$\ddot{q}_i(t) + 2\alpha_i \dot{q}_i(t) + (\omega_i^2 + \alpha_i^2)q_i(t) = \hat{Q}_i(t_{if}) \qquad (i = 1, 2, 3) \tag{26}$$

where $\hat{Q}_i(t_{if}) = \phi_i^T(x_\ell)\hat{U}(t_{if})\Delta_i$ is the $i$th modal impulse at time $t_{if}$. The solution to Eq. (26) is of the form

$$q_i(t) = e^{-\alpha_i t}[c_{i1} \cos(\omega_i t) + c_{i2} \sin(\omega_i t)] \qquad (i = 1, 2, 3) \tag{27}$$

where $c_{i1}$ and $c_{i2}$ are coefficients to be determined and $q_i(t_{if}) = \dot{q}_i(t_{if}) = 0$ are the final conditions. Solving the $i$th modal equation at $t_{if}$ yields

$$q_i(t_{if}) = \phi_i^T \hat{U}(t_0)\left[(1/\omega_i)e^{-\alpha_i t_{if}} \sin(\omega_i t_{if})\right] \tag{28}$$

$$\dot{q}_i(t_{if}) = \phi_i^T \hat{U}(t_0)\left\{e^{-\alpha_i t_{if}}[\cos(\omega_i t_{if}) - (\alpha_i/\omega_i)\sin(\omega_i t_{if})]\right\}$$
$$+ \phi_i^T \hat{U}(t_{if}) \tag{29}$$

in which we let $t_0 = 0$ without loss of generality. Applying the final conditions to Eq. (28) we find that $\omega_i t_{if} = n\pi$ $(n = 1, 2, \ldots)$ and that the $i$th modal impulse is

$$\hat{Q}_i(t_{if}) = (-1)^{n+1}\hat{Q}_i(0)e^{-\alpha_i t_{if}} \qquad (i = 1, 2, 3) \tag{30}$$

The actual impulses are determined from the modal impulses using Eqs. (20) and (30). The actual impulses are then approximated by finite duration and magnitude pulses as described later in the paper.

### Augmented Open-Loop In-Plane Maneuver

The fourth control approach augments IDC with the open-loop control of the preceding section. The IDC quenches residual elastic motion that is present due to unavoidable modeling uncertainties.
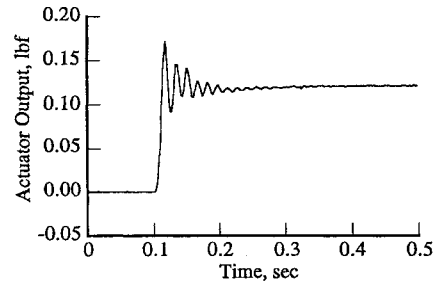
## V.   Air Thrust Actuation

The actuator thrust was measured as a function of supply line pressure via the calibration experiment depicted in Fig. 4a. The test apparatus consisted of an actuator fastened to two precision linear

Table 2   Typical air thrust actuator parameters, $P_s = 50$ psi

| | |
|---|---|
| Peak overshoot, % | 140 |
| Delay time, s | 0.003 |
| Rise time, s | 0.01 |
| Peak time, s | 0.014 |
| Settling time, s | 0.09 |
| Drop-off time, s | 0.006 |
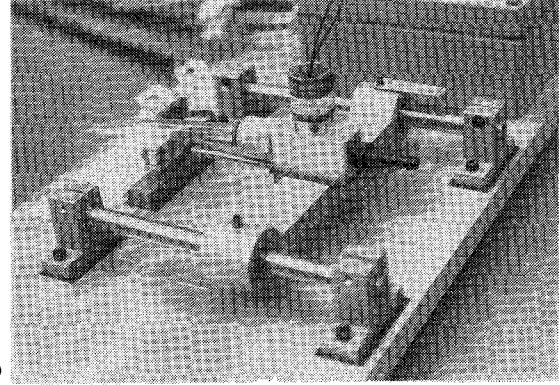




Fig. 4   Air thrust actuation calibration and characterization experiment: a) test apparatus, and b) typical air thrust response to step input with 0.1-s input delay.
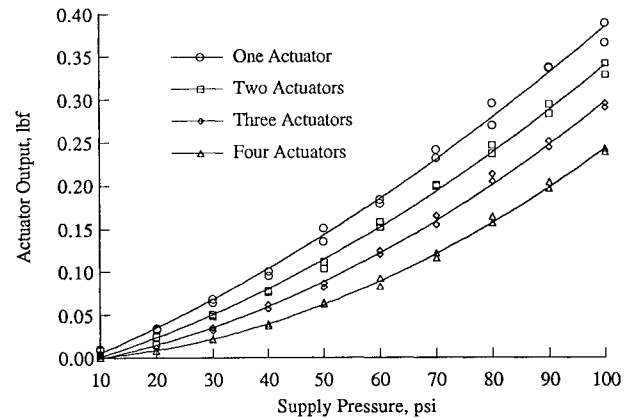


Fig. 5   Air thrust vs supply pressure for actuator combinations.

bearings riding on hardened steel rods. A load introduction bolt transmitted the actuator output to a 0.5-kg load cell. Air thrust activation timing and measurement were controlled by an Intel 80386-based microcomputer system that allowed for high-data collection rates relative to the beam's lowest three frequencies of oscillation. System characteristics determined from the calibration experiment are shown in Figs. 4b and 5 and Table 2.[28] Since multiple actuators would be operating simultaneously and using the same supply, it was necessary to calibrate actuator output in the presence of these conditions. It was determined that up to four actuators could be operating at one time, and so combinations of one, two, three, and four actuators were tested. Two sets of actuator test data were taken at

each supply pressure level for each possible combination of multiple actuators to determine steady-state thrust levels. The order of the tests was randomized in order to minimize any trend effects. The data shown in Fig. 5 were modeled by the equations

$$U_1 = 2.52956 \times 10^{-3} \cdot P_s + 1.54236 \times 10^{-5} \cdot P_s^2$$
$$10 < P_s < 100$$

$$U_2 = 1.74010 \times 10^{-3} \cdot P_s + 1.84717 \times 10^{-5} \cdot P_s^2$$
$$10 < P_s < 100$$

$$\tag{31}$$

$$U_3 = 9.41387 \times 10^{-4} \cdot P_s + 2.16310 \times 10^{-5} \cdot P_s^2$$
$$10 < P_s < 100$$

$$U_4 = 1.44317 \times 10^{-4} \cdot P_s + 2.32949 \times 10^{-5} \cdot P_s^2$$
$$10 < P_s < 100$$

where $U_j$ is the thrust of each actuator in pounds force with $j$ actuators operating simultaneously and $P_s$ is the supply pressure in pounds per square inch.

A modification to impulsive control is necessary since it is impossible to produce impulses exactly. In practice the instantaneous impulses must be converted into finite time pulses of duration $\Delta t$. Toward this end, the magnitudes of the impulse and of the finite duration pulse are equated[21]:

$$\int_{T_{1i}}^{T_{2i}} u_{\phi i} \, dt = \int_{T_{1i}}^{T_{2i}} \frac{c_i}{\alpha^*} \cdot \text{sgn}[g(\eta^*, \tau_i)] \delta(t - \tau_i) \, dt = \frac{c_i}{\alpha^*} \tag{32}$$

$$T_{2i} - T_{1i} = \Delta t_i = \frac{c_i}{\alpha^* \cdot u_i} \tag{33}$$

The time at which the pulse is initiated $T_{1i}$ depends on the prescribed impulse time $\tau_i$, the rise time of the actuators $t_r$, and the equivalent pulse duration $\Delta t_i$. We obtain

$$T_{1i} = \tau_i - t_r - (\Delta t_{ij}/2) \tag{34}$$

The final term in Eq. (34) centers the pulse over its prescribed impulse time. Another point to consider is that when the first pulse initiates the maneuver (at $t_0 = 0$) the pulse cannot be centered. To compensate, each successive pulse after the first is delayed by half of the duration of the first pulse. This results in a pulse of duration $\Delta t_i$ and of magnitude $u_i$ corresponding to the $i$th impulse in the solution to the fuel optimal control problem.

Equating impulse and pulse magnitudes reveals implications associated with the controller design. The first of these results is that for rigid-body maneuver the coast angular velocities are identical for both impulsive control and modified impulsive control. Second, the maneuver times for the modified impulsive approach are slightly larger than those for impulsive control due to acceleration and deceleration of the structure. Finally, the fuel consumptions associated with each approach are identical.

## VI. Rigid-Body and Elastic Sensing

The open-loop fuel-optimal control solution does not require measurements of the states; however, IDC requires measurements of the deflection and velocity of each of the beams at the actuator locations. Furthermore, measurements of the states were used to observe the performances of the four control systems developed. The states can all be extracted from the strain measurements and the angular rate measurements.

A strain gauge was placed on each beam where the beam joins the mount. The gauges were thin, flexible, and self-temperature compensating. A high resistance of 350 $\Omega$ was selected to increase the signal-to-noise ratio. The transverse sensitivity was low (0.8% $\pm$ 0.2%) to reduce the corruption of the pure bending component by torsional effects. The measured elastic displacement of the $j$th beam relative to a line tangent to the beam at its root is expressed in the form of a cubic function $w_{mj}(x_j, t)$ and we impose the boundary conditions

$$w_{mj}(0, t) = \frac{\partial w_{mj}(0, t)}{\partial x} = \frac{\partial^2 w_{mj}(L, t)}{\partial x^2} = 0$$
$$\frac{\partial^2 w_{mj}(0, t)}{\partial x^2} = \Gamma_j(t) \tag{35}$$

where $\Gamma_j(t)$ is the $j$th beam's curvature at the root and $w_{mj}(x_j, t)$ the measured elastic displacement of the $j$th beam at $x_j$. We obtain the form

$$w_{mj}(x_j, t) = \frac{\Gamma_j(t)}{6L} x_j^3 - \frac{\varepsilon_j(t)}{T} x_j^2, \qquad \Gamma_j(t) = -\frac{2\varepsilon_j(t)}{T} \tag{36}$$

where $\varepsilon_j(t)$ is the measured strain, $L$ the length of each beam, and $T$ the thickness. The time rates of change of $w_{mj}(x_j, t)$ were computed by a backward finite difference.

The angular rate transducer located on the rotation mount provided voltage output linearly proportional to the angular rate input of $\phi$, $\theta$, and $\psi$ with minimal cross-axis coupling. Hysteresis was essentially zero with a slow transient shift of the null signal typically $\pm 1\%$ of full scale. The 12-bit data acquisition restricted input resolution to $1.221 \times 10^{-3}$ deg/s. The unit threshold was approximately 0.01 deg/s with a maximum measured rate of 180 deg/s. Angular position measurements were extracted by numerical integration.

## VII. Results and Discussion

The sampling frequency in each of the experiments was 100 Hz, and supply pressures were kept high to more accurately approximate impulses. The tip displacement profiles are located at tip 1 of the structure. They are typical of the other tip displacements. The analytically predicted natural frequencies and the measured natural frequencies are compared in Table 3. The experimentally measured frequencies were obtained by imparting initial conditions on the structure by a pulse fired from one of the in-plane actuators. The pulse excited the in-plane rigid-body mode as well as several elastic modes. Free response strain measurements, Fig. 6a, were used to calculate the power spectral density shown in Fig. 6b.

**Table 3  Comparison of predicted and measured natural frequencies, Hz**

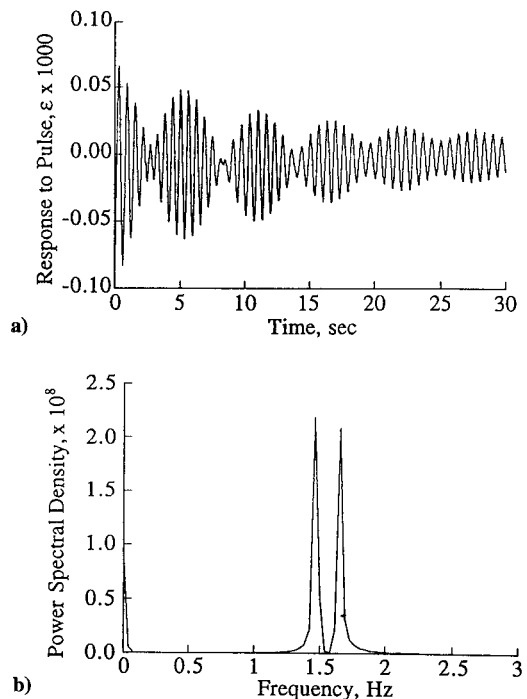| Frequency | Predicted | Measured |
|---|---|---|
| $\omega_1$ | 1.480 | 1.476 |
| $\omega_2, \omega_3$ | 1.658 | 1.650 |



a)



b)

**Fig. 6  Pulse response and measured natural frequencies: a) free response strain measurements, and b) calculated power spectral density.**
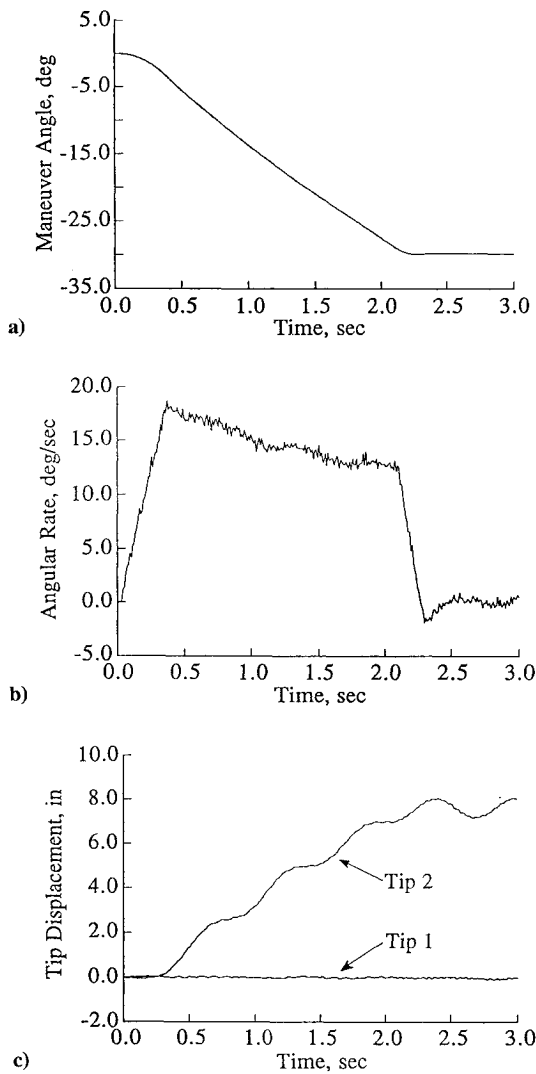
**Fig. 7  Open-loop out-of-plane maneuver: a) maneuver angle profile, b) angular rate profile, and c) tip displacement.**

Figure 7 shows the results from the out-of-plane open-loop pitch maneuver. The maneuver was designed to rotate the structure −30 deg in 2 s. The supply pressure for this experiment was 75 psi, which resulted in an actuator thrust of 0.28 lbf. Figure 7a shows the maneuver angle profile, illustrating the expected acceleration and deceleration of the structure. As expected, a slightly larger maneuver time than predicted was obtained. This is a consequence of using pulses to approximate the prescribed impulses. Figure 7b shows the angular rate profile of the structure and illustrates the effect of hinge friction which results in decreasing velocity during the coasting portion of the maneuver. Figure 7c shows the tip displacements of two orthogonal members during the maneuver. Tip 1, as identified in Fig. 2, experiences negligible deflection, whereas tip 2 deflects almost 8 in. by completion of the maneuver. This illustrates the unavoidable presence of static deflections encountered when dealing outside the plane normal to gravity.

Figures 8a–8d show the in-plane maneuver results obtained by the hybrid controller. The maneuver was designed to rotate the structure 90 deg in 5 s. The supply pressure was again 75 psi. In this case, one air jet initiated and terminated the rigid-body portion of the maneuver and two opposing jets quenched the vibration upon completion of the maneuver. The jet selection was based on minimizing drift effects during the elastic motion control portion of the maneuver. In this case, instances of local peak velocity and local minimum displacement coincided so that only the displacement was used to determine the actuator state, whereas the velocity was used to determine thrust direction. Because of this simplification, no velocity deadband level and standard deviation gain were required.
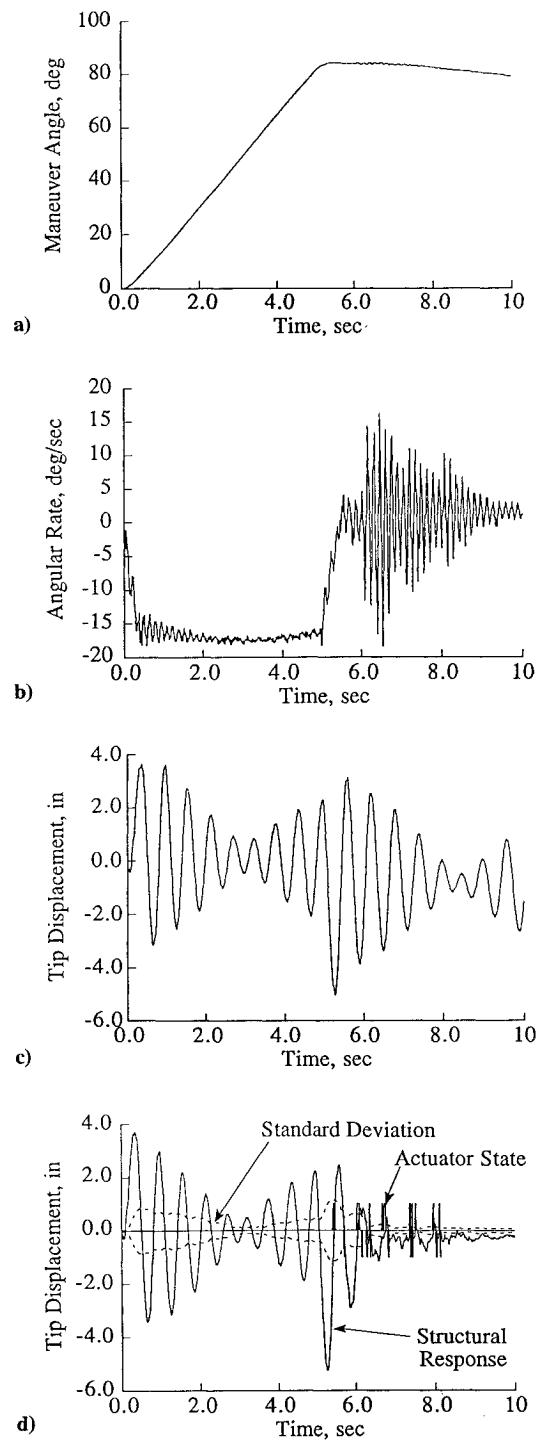


**Fig. 8  Hybrid in-plane maneuver: a) maneuver angle profile, b) angular rate profile, c) uncontrolled tip displacement, and d) controlled tip displacement.**

The displacement gain $\mu_{wj}$ was 0.3 and the displacement deadband level was 1.0 in. The running-in-time standard deviation window size was selected to be one-half the period of the lowest participating mode, which was 0.34 s. By selecting a window size equivalent to integer increments of the lowest frequency's half-period, oscillations in the standard deviation can be minimized.[29] The maneuver angle profile in Fig. 8a shows that the structure fell short of its target by approximately 4 deg. This is due to the increased hinge friction effects resulting from the structures oscillations during the coasting phase of the maneuver. Figure 8b shows the angular rate profile and displays high-frequency oscillations excited when the elastic body controller is engaged. Figure 8c shows the tip displacement of the structure if allowed to oscillate freely at the completion of the maneuver, and Fig. 8d shows the controlled profile. Indicated in Fig. 8d
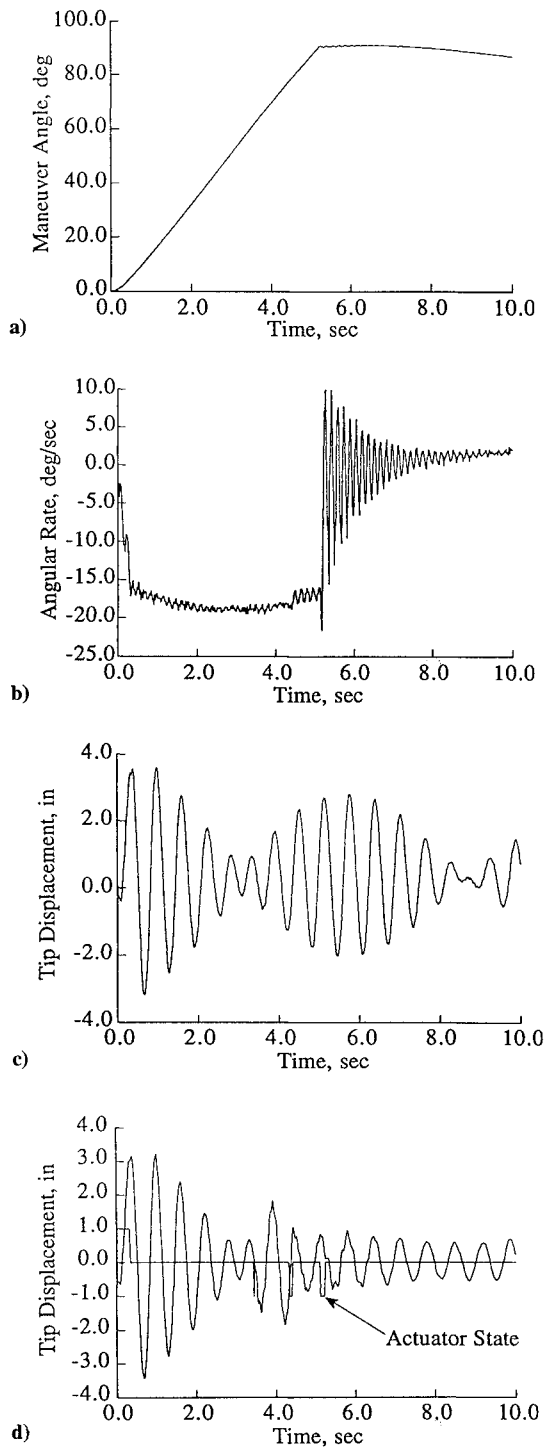
**Fig. 9 Open-loop in-plane maneuver: a) maneuver angle profile, b) angular rate profile, c) uncontrolled tip displacement, and d) controlled tip displacement.**



**Fig. 10 Augmented open-loop in-plane maneuver: a) maneuver angle profile, b) angular rate profile, and c) tip displacement.**

are the running-in-time standard deviation and the actuator state. A slight static deflection is noticed in the terminal portion of the profile due to gravity affects caused by a slight skewing of the X plane.

Figures 9a–9d show the results from the in-plane maneuver using the open-loop controller. The maneuver was again designed to rotate the structure 90 deg in 5 s, but in this case a supply pressure of 85 psi was used to more accurately approximate the prescribed impulses. Four modes were determined to significantly participate in the response of the structure, one rigid-body rotation and three elastic-body modes. Two pulses were prescribed to initiate and then terminate the contribution of each of the modes. The initial pulses for each of the modes was at $t = 0$, and it was concluded that the second and third elastic-body modes would be quenched simultaneously so four separate pulses resulted. The first pulse employed a single jet
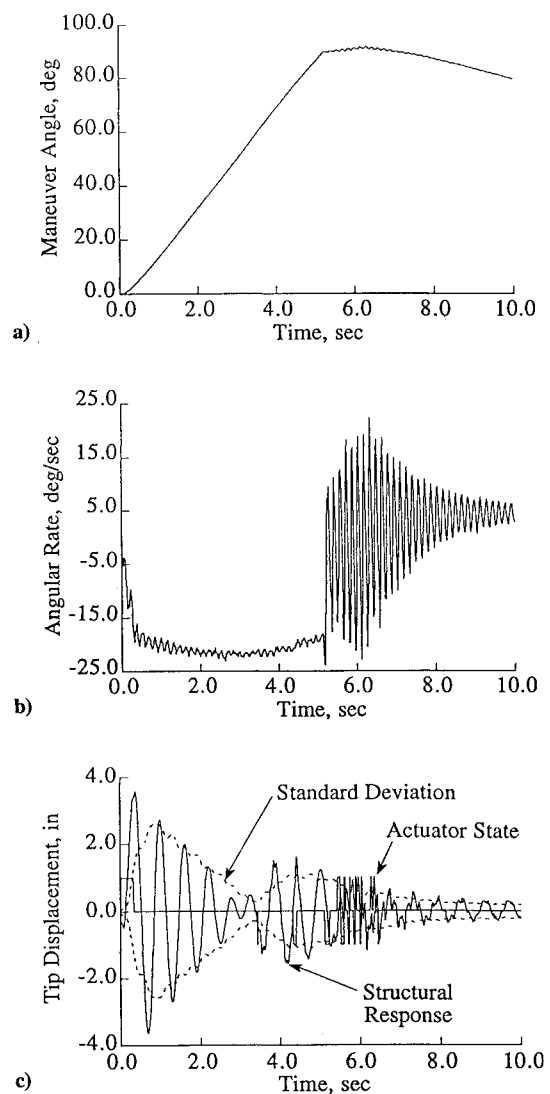
that initiated the rigid-body maneuver and excited the first three elastic modes. The second pulse used all four in-plane jets and was designed to remove the first elastic mode after 10 periods of oscillation. The third pulse was designed to remove the second and third elastic modes simultaneously after 14 periods of oscillation. Only two actuators were required for the third pulse due to the symmetry of the second and third modes. The fourth pulse again used all four in-plane jets and removed the rigid-body mode from the maneuver. The pulse times used to quench the elastic modes were determined such that the natural damping of the system could be employed to reduce the required fuel and so that the pulses could be separated and distinguishable. Figure 9a shows the maneuver angle profile and Fig. 9b shows the angular rate time history. The maneuver angle was within 2 deg of the prescribed maneuver, whereas the angular rate shows the same high-frequency characteristics as the previous case. Figure 9c shows the free elastic response of the structure if only the first pulse is employed, and Fig. 9d shows the controlled case including the actuator pulse profile. It should be noted that only a small component of the first elastic mode remains after termination of the maneuver. This is due to errors in the analytical mode shapes used in determining the pulse magnitudes.

Figures 10a–10c show the results from the in-plane maneuver using the augmented open-loop controller. It was attempted to increase the performance of the open-loop controller by implementing the fuel near optimal technique of IDC after completion of the open-loop control. In this experiment, two opposing actuators were employed during the additional elastic control phase. A supply pressure of 85 psi was again used along with a $\mu_{wj}$ of 0.7 and a displacement

deadband level of 1.0 in. The standard deviation window size was again 0.34 s in width. Figure 10a shows a residual drift in the maneuver angle that is due to unbalanced jet participation in the closed-loop elastic control phase. Figure 10b shows slightly larger amplitudes in the higher modes that are excited during rapid pulsing of the jets. Figure 10c shows the tip displacement profile for the augmented open-loop controller. It is seen that the residual amplitude is decreased by almost 50% from the open-loop controller.

## VIII. Conclusions

Structural flexibility has posed problems in the design of control systems used to maneuver and suppress the vibration of large flexible space structures. Until recently, experimental verification of these control approaches has trailed behind the theoretical developments. The experiment reported on in this paper was developed to verify new techniques in fuel and time optimal control of flexible space structures. The spacelike dynamics of the experimental structure comprise several rigid- and elastic-body modes. Air-fed reaction control jets were used for both maneuver and vibration suppression and the structure's weight was minimized to maintain high-control authority.

Four fuel optimal control approaches for the propulsive maneuver of space structures were examined. The first was a fuel optimal open-loop out-of-plane maneuver that demonstrated effects due to operating in a gravity environment. A hybrid controller was implemented next that performed an in-plane rest-to-rest maneuver and showed excellent vibration suppression performance. The third approach applied a fuel optimal open-loop control to the rest-to-rest maneuver problem and illustrated difficulties in implementation in the presence of modeling errors. The fourth approach improved the performance of the third by augmenting the open-loop control with a near fuel optimal vibration suppression technique.

## Acknowledgments

## References

[1]Williams, J. P., "Status Report and Preliminary Results of the Spacecraft Control Laboratory Experiment," Proceedings of the Structural Dynamics and Control Interaction of Flexible Structures, NASA CP 2467, Pt. 1, 1986, pp. 359–397.

[2]Das, A., Slimak, L. K. S., and Schlaegel, W. T., "Spacecraft Dynamics and Control Program at AFRPL," Proceedings of the First NASA/DOD CSI Technology Conference (Norfolk, VA), NASA, 1986, pp. 25–40.

[3]Das, A., "Large Angle Maneuver Experiments in Ground-Based Laboratories," Proceedings of the 1990 AIAA Dynamic Specialist Conference, AIAA, Washington, DC, 1990 (AIAA Paper 90-1236).

[4]Sparks, D. W., and Juang, J., "Survey of Experiments and Experimental Facilities for Control of Flexible Structures," Journal of Guidance, Control, and Dynamics, Vol. 15, No. 4, 1992, pp. 801–816.

[5]Peterson, L. D., "Optimal Projection Control of an Experimental Truss Structure," Journal of Guidance, Control, and Dynamics, Vol. 14, No. 2, 1991, pp. 241–250.

[6]Wie, B., Horta, L., and Sulla, J., "Classical Control System Design and Experiment for the Mini-MAST Truss Structure," Journal of Guidance, Control, and Dynamics, Vol. 14, No. 4, 1991, pp. 778–784.

[7]Schamel, G. C., II, and Haftka, R. T., "Active Vibration Control with Model Correction on a Flexible Laboratory Grid Structure," Journal of Guidance, Control, and Dynamics, Vol. 14, No. 5, 1991, pp. 993–1000.

[8]Bruner, A. M., Belvin, W. K., Horta, L. G., and Juang, J.-N., "Active Vibration Absorber for the CSI Evolutionary Model: Design and Experimental

Results," Journal of Guidance, Control, and Dynamics, Vol. 15, No. 5, 1992, pp. 1253–1257.

[9]Collins, E. G., Jr., King, J. A., Phillips, D. J., and Hyland, D. C., "High Performance, Accelerometer-Based Control of the Mini-MAST Structure," Journal of Guidance, Control, and Dynamics, Vol. 15, No. 4, 1992, pp. 885–892.

[10]Wie, B., "Experimental Demonstration of a Classical Approach to Flexible Structure Control," Journal of Guidance, Control, and Dynamics, Vol. 15, No. 6, 1992, pp. 1327–1333.

[11]Dunn, H. J., "Experimental Results of Active Control on a Large Structure to Suppress Vibration," Journal of Guidance, Control, and Dynamics, Vol. 15, No. 6, 1992, pp. 1334–1341.

[12]Ih, C.-H. C., Bayard, D. S., Ahmed, A., and Wang, S. J., "Experiments in Multivariable Adaptive Control of a Large Flexible Structure," Journal of Guidance, Control, and Dynamics, Vol. 16, No. 1, 1993, pp. 9–13.

[13]Ih, C.-H. C., Bayard, D. S., Ahmed, A., and Wang, S. J., "Experimental Study of Robustness in Adaptive Control for Large Flexible Structures," Journal of Guidance, Control, and Dynamics, Vol. 16, No. 1, 1993, pp. 14–20.

[14]Redmond, J., Meyer, J. L., and Silverberg, L., "Impulse Damping Control of an Experimental Structure," Journal of Sound and Vibration, Vol. 160, No. 1, 1993, pp. 179–186.

[15]Williams, J. P., "Slewing Maneuvers on the SCOLE Laboratory Facility," Proceedings of the First NASA/DOD CSI Technology Conference, NASA, 1986, pp. 851–867.

[16]Shenhar, J., Sparks, D., Jr., Williams, J. P., and Montgomery, R. C., "Attitude Control System Testing on SCOLE," Proceedings of the Sixth VPI&SU Symposium on Dynamics and Control of Large Structures (Blacksburg, VA), 1987, pp. 251–273.

[17]Brown, M. E., "Rapid Slewing Maneuvers of a Flexible Spacecraft Using On/Off Thrusters," M.S. Thesis, Dept. of Aeronautics and Astronautics, Massachusetts Inst. of Technology, Cambridge, MA, Sept. 1983.

[18]Floyd, M. A., "Single-Step Optimal Control of the RPL Experiment," Advances in the Astronomical Sciences, Vol. 57, 1985, pp. 323–350.

[19]Bossi, J. A., and Tsou, J. W., "A Laboratory Experiment in Control/Structure Interaction," Proceedings of the 1986 American Control Conference, Inst. of Electrical and Electronics Engineers, 1986, pp. 1034–1038.

[20]Junkins, J. L., Rahman, Z. H., and Bang, H., "Near-Minimum-Time Control of Distributed Parameter Systems: Analytical and Experimental Results," Journal of Guidance, Control, and Dynamics, Vol. 14, No. 2, 1991, pp. 406–415.

[21]Silverberg, L. M., and Meyer, J. L., "Fuel Optimal Slewing of an Experimental Hinged-Free Beam," Journal of Guidance, Control, and Dynamics, Vol. 16, No. 6, 1993, pp. 1162–1168.

[22]Redmond, J., and Silverberg, L., "Fuel Consumption in Optimal Control," Journal of Guidance, Control, and Dynamics, Vol. 15, No. 2, 1992, pp. 424–430.

[23]Silverberg, L., and Redmond, J., "Fuel-Optimal Propulsive Reboost of Flexible Spacecraft," Journal of Guidance, Control, and Dynamics, Vol. 16, No. 2, 1993, pp. 294–300.

[24]Foster, L. A., and Mapar, J., "Control Structure Interaction for Space Station Freedom Early Assembly Flights," Proceedings of the AAS/AIAA Spaceflight Mechanics Meeting (Houston, TX), American Astronomical Society, 1991 (AAS Paper 91-146).

[25]Silverberg, L., "Light Impulsive Damping of Spacecraft Exhibiting Normal Mode Behavior," Journal of Guidance, Control, and Dynamics, Vol. 15, No. 1, 1992, pp. 114–120.

[26]Meirovitch, L., Computational Methods in Structural Dynamics, Sijthoff and Noordhoff, Alphen aan den Rijn, The Netherlands, 1980, pp. 285–327.

[27]Shenhar, J., and Meirovitch, L., "Minimum Fuel Control of Higher Order Systems," Journal of Optimization Theory and Applications, Vol. 48, No. 3, 1986, pp. 469–491.

[28]Hale, F. J., Introduction to Control System Analysis and Design, Prentice–Hall, Englewood Cliffs, NJ, 1973, pp. 17–20.

[29]Meyer, J. L., "Experimental Verification of Impulse Damping Control," M.S. Thesis, Dept. of Mechanical and Aerospace Engineering, North Carolina State Univ., Raleigh, NC, May 1990.